Research Square

Preprints are preliminary reports that have not undergone peer review. They should not be considered conclusive, used to inform clinical practice, or referenced by the media as validated information.

Physics-Informed Multiscale Modeling of High-Bandwidth Electrohydraulic Actuator Dynamics

A S Sharraan

sharanaj17@gmail.com

Bapuji Institute of Engineering and Technology

G Manavendra

Bapuji Institute of Engineering and Technology

S. P Shivakumar

S.J.M Institute of Technology,

P. B Bharath

S.J.M Institute of Technology,

H V Anand

DMG MORI India Pvt. Ltd.,

Research Article

Keywords: Electrohydraulic actuator, Servo valve, Transitional flow, Discharge coefficient, Computational fluid dynamics, Reduced-order modeling, Transient fluid inertia, Hardware-in-the-loop, Digital twin

Posted Date: October 21st, 2026

DOI: https://doi.org/10.21203/rs.3.rs-10866006/v1

License: This work is licensed under a Creative Commons Attribution 4.0 International License. Read Full License

Additional Declarations: No competing interests reported.

Physics-Informed Multiscale Modeling of High-Bandwidth Electrohydraulic Actuator Dynamics

A S Sharraan [1], G Manavendra [2] , S. P Shivakumar [3], P.B Bharath[4] Mr. Anand H V[5]

[1&2]*Department of Mechanical Engineering*

Bapuji Institute of Engineering and Technology, Davangere-577004 Karnataka, India

[3&4]*Department of Mechanical Engineering*

S.J.M Institute of Technology, Chitradurga-577502 Karnataka, India

[5] *DMG MORI India Pvt. Ltd., Bangalore - 560058Karnataka, India*

E-mail: sharanaj17@gmail.com

Tel: +9198446 16304; Fax: +918192 223261

Abstract

Predicting high-bandwidth electrohydraulic actuator dynamics is often limited by two simplifying assumptions: constant discharge coefficient and neglect of transient fluid inertia. This work addresses both within a unified multi-scale framework. At the micro scale, 112 CFD simulations are used to develop a regime-aware closed-form correlation for $C_d(R_e)$ spanning laminar, transitional, and turbulent flow, with R^2=0.978. At the meso scale, transient fluid inertia is coupled with jet-momentum flow force. At the macro scale, these effects are incorporated into a reduced-order motor–spool–line model for real-time implementation. Validation on a direct-drive pilotless prototype, using laboratory tests, hardware-in-the-loop simulation, and operating-condition emulation, shows magnitude errors below 5% over 1–800 Hz, bandwidth and natural-frequency errors within ±3.2%, and phase errors below 10° up to 600 Hz. Ablation results indicate that assuming constant C_d increases displacement error by 50% and phase-margin loss by up to 18°, neglecting transient inertia increases error by 28%, and omitting both increases error by 125%. The prototype achieves a 950 Hz natural frequency and a 650 Hz closed-loop −3 dB bandwidth. These results demonstrate that physics-informed multi-scale coupling is critical for predictive design and digital-twin deployment of next-generation high-bandwidth electrohydraulic systems.

Keywords: Electrohydraulic actuator; Servo valve; Transitional flow; Discharge coefficient; Computational fluid dynamics; Reduced-order modeling; Transient fluid inertia; Hardware-in-the-loop; Digital twin.

Nomenclature

Symbol	Description	Unit
A	Geometric orifice area	m^2
A_s	Pressure-sensitive spool area	mm^2
B_m	Motor friction coefficient	N·m·s/rad
B_s	Spool damping coefficient	N·s/m
C_d	Discharge coefficient	–
$C_d(Re)$	Regime-aware discharge coefficient correlation	–
C_{line}	Line compliance	m^3/Pa
d_H	Hydraulic diameter	μm
F_x	Axial flow force	N
h	Orifice opening height	mm
J_m	Motor rotor inertia	kg·m^2
K_b	Back-EMF constant	V·s/rad
K_f	Flow-force damping coefficient	N·s/m
K_h	Hydraulic stiffness	N/m
K_m	Motor torque constant	N·m/A
K_s	Return-spring stiffness	N/m
L_a	Armature inductance	mH
L_e	Effective fluid-column length	m
M_t	Equivalent lumped transient fluid inertia	kg

Symbol	Description	Unit
M_{eff}	Effective spool mass	kg
P	Wetted perimeter	m
ΔP	Orifice pressure drop	Pa
Q	Volumetric flow rate	L/min
Re	Reynolds number	–
R_{a}	Armature resistance	Ω
R_{line}	Line resistance	bar/(L/s)
V_{a}	Armature voltage	V
w	Slot width	mm
x_{v}	Spool displacement	mm
Z_{line}	Line impedance	Pa·s/m^5
θ	Jet deflection angle	deg
ρ	Fluid density	kg/m^3
μ	Dynamic viscosity	Pa·s
ω_{n}	Natural frequency	rad/s
ζ	Damping ratio	–

1. Introduction

1.1 Background and motivation

Electrohydraulic actuators (EHAs) remain indispensable wherever high force density, stiffness, and bandwidth must be delivered simultaneously, most prominently in aerospace flight control, precision manufacturing, and robotic manipulation [1–4]. Despite sustained advances in electromechanical actuation, electrohydraulic servo valves retain superior power-to-weight ratios and dynamic response in bandwidth-critical regimes [5–8]. Exploiting the full performance envelope of modern EHAs, however, requires accurate prediction of the flow-metering physics inside servo-valve orifices, at length scales where conventional macro-scale assumptions cease to hold.

At the hydraulic diameters characteristic of precision metering geometries (d_H = 20–500 μm), Reynolds numbers routinely span Re = 100–5000 during fine positioning tasks. Across this range the discharge coefficient varies non-monotonically from approximately 0.50 to 0.63, governed by Reynolds number, orifice edge geometry, and the formation dynamics of the vena contracta [9–14]. A 10% deviation in C_d at $Re < 500$ can erode closed-loop phase margin by more than 15°, a loss sufficient to destabilize control loops targeting bandwidths above 100 Hz [15–17]. Compounding this error, transient fluid inertia, routinely neglected in quasi-steady formulations, becomes a first-order contributor to spool dynamics above roughly 50 Hz, where rapid pressure transients during high-rate maneuvers generate reaction forces proportional to $\mathrm{d}Q/\mathrm{d}t$ [18–20]. Its omission systematically underpredicts flow forces, by up to 28% in root-mean-square terms in the present study, consistent with reported identification errors in servo-hydraulic systems [21, 22]. For high-bandwidth applications, the nonlinear amplification of micro-scale metering errors into macro-scale instability constitutes a critical, and hitherto unresolved, modeling gap.

1.2 The scale-coupling challenge

Accurate EHA modeling requires rigorous coupling across three physically distinct scales.

Micro scale (orifice metering physics). As surface forces grow relative to inertial forces, viscous boundary layers occupy 70–90% of the micro-orifice cross-section, and precision-machining striations and edge imperfections critically modulate the vena contracta topology. Regime-aware $C_d(Re)$ characterization is therefore required to capture the non-monotonic laminar-to-turbulent transition that constant-$C_d \approx 0.61$ formulations cannot represent.

Meso scale (flow-force generation). The axial flow force on the valve spool comprises two mechanisms described by the Reynolds transport theorem:

$$F_x = \rho Q v_{jet} \cos\theta + \rho L_e \, \mathrm{d}Q/\mathrm{d}t \tag{1}$$

where the first term is the steady jet-momentum force and the second captures transient fluid inertia [18–20]. In miniaturized servo valves, small fluid volumes and short column lengths produce extremely rapid pressure transients, elevating the transient-inertia term from a secondary correction to a primary dynamic contribution. Omitting it systematically underpredicts flow forces and distorts the identified spool dynamics [21, 22].

Macro scale (system-level dynamics). Hydraulic transmission lines, compliant packaging, and structural resonances form lightly damped impedance networks whose coupling with the valve produces gain peaking and phase degradation inside the operational bandwidth [23–27]. Reduced-order surrogates that capture this coupling are essential for system-level co-design of actuator geometry, fluidic interconnects, and embedded control architecture [28–31], yet most existing models treat orifice physics, flow forces, and system dynamics as decoupled sub-problems.

This scale-coupling paradox, in which the physics most commonly neglected in industrial models becomes most consequential at precision-control scales, is the central scientific motivation of this work.

1.3 Research gap and contributions

This study bridges micro-scale flow physics and macro-scale actuator dynamics through a unified micro–meso–macro predictive simulation framework, validated experimentally on a representative direct-drive pilotless actuator. The proposed methodology resolves long-standing discrepancies in discharge-coefficient assumptions and transient-inertia modeling. The specific contributions are as follows.

(1) **A regime-aware, closed-form discharge correlation suitable for real-time embedding.** A systematic campaign of 112 high-fidelity CFD simulations spanning Re = 100–5000 yields a continuous algebraic correlation for $C_d(Re)$ ($R^2 = 0.978$). Unlike look-up tables or iterative solvers, the formulation is computationally trivial and can be embedded directly in real-time control architectures and reduced-order digital twins.

(2) **A multi-scale physics-coupling methodology.** A rigorous coupling strategy propagates the CFD-derived $C_d(Re)$ correlation and the Reynolds-transport transient-fluid-inertia term seamlessly from the micro-orifice scale to macro-scale mass–spring–damper dynamics, capturing the Reynolds-number-dependent stiffness and damping variations that constant-C_d models fundamentally miss.

(3) **Rigorous triple-domain verification and validation.** Following ASME V&V 20 and ISO GUM practice, closed-loop frequency-response predictions match measurements within 5% in magnitude over 1–800 Hz, within ±3.2% in natural frequency and bandwidth, and within 10° in phase up to 600 Hz. Comprehensive ablation studies isolate the individual physical contributions and confirm quantitatively that both regime-aware metering and transient fluid inertia are indispensable for accurate stability prediction.

(4) **Quantitative decomposition of bandwidth-limiting mechanisms.** The framework decomposes dynamic performance limits into physically identifiable sources, providing actionable design targets for next-generation actuators.

(5) **Generalizability through scale-closure analysis.** Dimensional scaling analysis shows that the framework's core physics, namely regime-dependent discharge, transient fluid inertia, and flow-force coupling, grow in significance as device dimensions shrink toward precision scales, establishing a methodological pathway across disparate length scales.

2. Literature review

2.1 Electrohydraulic actuation and modeling

The foundational treatments of Merritt [32] and Blackburn et al. [33] established quasi-steady orifice-flow models with a constant discharge coefficient ($C_d \approx 0.61$) that have dominated hydraulic control practice for seven decades. These models presume fully turbulent flow, a condition rarely satisfied in precision servo valves whose metering orifices traverse the laminar and transitional regimes [10, 12, 13]. Recent evidence underscores the stability consequences of this simplification: Zhao et al. [15] showed that discharge-coefficient modeling errors directly degrade stability margins in electrohydraulic systems, and Li et al. [13] measured pronounced C_d variation across Reynolds number in hydraulic spool valves. In parallel, a substantial control literature has produced nonlinear adaptive, robust, gain-scheduled, and sliding-mode designs for electrohydraulic systems [16–19, 34, 35]; these controllers, however, typically inherit the constant-C_d plant model, leaving the underlying physics gap unresolved.

2.2 Computational fluid dynamics in valve design

CFD has become an essential tool for valve design and optimization. Lisowski and co-workers analyzed flow forces under cavitating conditions [36] and in proportional valves with rectangular metering edges [37], while Nishida and Ivantysynova examined under-lapped and overlapped metering configurations [38]. Vacca et al. [39] and Chen et al. [40] developed numerical approaches for steady-state flow-force evaluation, later extended to large-flow valves [41] and to energy-loss characterization [42], and Wang et al. [14] resolved transitional flow inside a spool valve. These studies focus predominantly on static characterization and do not address the transient-inertia effects that govern high-frequency dynamic prediction.

2.3 Multi-scale modeling and system identification

The need for approaches that bridge CFD and system-level dynamics is increasingly recognized. Rossi and Vacca [43] presented multi-scale modeling from CFD to system dynamics, Garcia et al. [44] developed predictive commissioning methodologies for high-bandwidth hydraulic systems, and Liang et al. [45] proposed physics-informed digital twins for valve prognostics; co-simulation workflows [28] and component-level design studies [29–31] have further broadened the toolset. System identification has likewise evolved from black-box neural networks toward physics-informed formulations [46, 47, 49], including long short-term memory predictors for direct-drive servo valves [48]. What remains missing, as recently emphasized in a survey of the seventy-year modeling gap [50], is a unified micro–meso–macro coupling with an explicit, closed-form metering closure that ensures extrapolation safety across the operating envelope.

2.4 Positioning of the present work

Table 1 situates the proposed framework relative to existing methodologies. Unlike prior approaches, this work integrates regime-aware $C_d(Re)$ physics, a transient-inertia closure, and real-time reduced-order modeling within a single, experimentally validated framework.

3. Representative electrohydraulic actuator architecture

3.1 System architecture

The experimental platform is a direct-drive electrohydraulic actuator designed to reproduce the dynamic characteristics of high-bandwidth servo systems (Fig. 1). A 12 V DC servo motor (Maxon) is coupled directly, through a low-inertia aluminum shaft, to a hardened-steel spool (10 mm diameter, 0.5 mm metering slots, 0–3.5 mm travel) fitted with return springs for fail-safe centering. The valve body is an ISO 4401-05-compliant NG10 four-way, three-position spool valve [55] mounted on a vibration-damped aluminum plate; the manifold is rated for 21 MPa with an 18 MPa pilot relief.

The direct-drive architecture eliminates the hydraulic pilot stage entirely. This is particularly advantageous for precision control, where pilot-stage stiction, supply-pressure sensitivity, and internal leakage paths are documented sources of dynamic anomalies and in-service degradation [8, 51–54]. The single-stage design achieves (i) elimination of pilot-stage stiction, a documented source of phase-margin erosion; (ii) removal of sensitivity to pilot-supply pressure fluctuation; (iii) a 5–20× reduction

in internal leakage paths; and (iv) a 27% volume reduction relative to conventional two-stage servo valves.

Fig. 1. Conceptual illustration of the pilotless electrohydraulic actuator showing physics propagation from the micro to the macro scale. The cross-section reveals the servo valve (with CFD mesh), where the laminar-to-turbulent transition occurs across the Reynolds-number spectrum (Re = 100–5000); the transition zone (Re = 300–3000) coincides with the range in which precision positioning tasks operate. The electric motor drives the spool against an integrated position sensor, enabling high-bandwidth closed-loop control (natural frequency ≈ 950 Hz) through the unified micro–meso–macro modeling framework. Color-coded flow visualization illustrates how micro-scale physics propagates into macro-scale stability.

3.2 Electronics and control interface

A microcontroller executes supervisory control through a relay H-bridge, driving the servo motor (K_m = 0.086 N·m/A) with 500 Hz pulse-width modulation. The direct-drive configuration provides linear current-to-displacement coupling without gain scheduling. The user interface comprises a 4×4 keypad and a 16×2 LCD; RS-232 logging provides data acquisition at 9600 baud. Isolated 5 V/12 V rails with Li-ion backup, thermal shutdown (>80 °C), and overcurrent protection ensure operational safety. An external data-acquisition system (National Instruments CompactDAQ, 16-bit, hardware-synchronized) characterizes the frequency response to 800 Hz, exceeding the Nyquist requirement for identifying the 650 Hz closed-loop bandwidth. The experimental arrangement is shown in Fig. 2.

Fig. 2. Experimental setup for the pilotless electrohydraulic actuator, comprising a DC servo motor mechanically coupled to a Bosch directional control valve. Key components: (1) DC servo motor for spool actuation; (2) precision mechanical coupling; (3) four-way directional control valve with standard ISO 4413 ports (P = pressure, T = tank, A/B = work ports). The system enables micro-positioning of the spool (resolution < 1 μm) for valve characterization across Re = 100–5000, supporting the micro–meso–macro modeling framework presented in this work.

3.3 Instrumentation and physical parameters

High-fidelity instrumentation ensures accurate state reconstruction. Table 2 summarizes the geometric, hydraulic, and electromechanical parameters of the platform.

4. Unified multi-scale modeling framework

4.1 Framework overview

The framework predicts dynamic performance by integrating physics across three scales: (i) at the micro scale, high-fidelity CFD resolves laminar-to-turbulent flow at sub-millimetre openings (h = 0.3–3.5 mm, Re = 100–5000) and yields a regime-aware $C_d(Re)$ correlation; (ii) at the meso scale, the Reynolds transport theorem provides the axial spool force, comprising steady jet momentum and transient fluid inertia; and (iii) at the macro scale, coupled motor electromechanics, spool dynamics, and line impedance yield time- and frequency-domain response with quantifiable stability margins.

4.2 Micro-scale CFD modeling

4.2.1 Computational domain and setup

A sharp-edged rectangular micro-orifice (L = 1.0 mm, d = 0.5 mm, w = 10 mm), representative of servo-valve metering slits, was modeled in ANSYS Fluent 2023R2. The domain included upstream and downstream chambers with reference planes located at least four hydraulic diameters from the orifice to ensure fully developed boundary conditions. Structured meshes with $y^+ \leq 1$ inflation layers and fifteen divisions across the orifice throat resolved the boundary layer.

Mesh independence was verified through Grid Convergence Index (GCI) analysis across coarse (8,000-element), medium (18,000-element), and fine (35,000-element) meshes. At the critical transitional Reynolds number (Re = 2000), the deviation in C_d and ΔP between the medium and fine meshes remained below 0.4% (Table 3), and the medium mesh was adopted for the production campaign.

Simulations used ISO VG 46 hydraulic oil (ρ = 860 kg/m^3, μ = 0.03 Pa·s). Regime-adaptive turbulence modeling was employed: a laminar closure for $Re < 500$, the γ–Re_θ transition model for $500 \leq Re \leq 2000$, and the k–ε model for $Re > 2000$. Convergence was enforced with residuals below 10^{-5} and mass-flow-rate stability below 0.1% over the final 500 iterations. Representative transitional-regime flow physics are shown in Fig. 3.

Fig. 3. Transitional-regime flow physics: vena contracta formation at Re = 1500. Velocity streamlines and magnitude contours for ISO VG 46 hydraulic oil through the 1.0 mm orifice show jet acceleration to 5.9 m/s, followed by downstream turning and boundary-layer development. Clear vena contracta formation validates the medium mesh (18,000 elements, GCI < 0.3%, Table 3) for discharge-coefficient

prediction (C_d = 0.614 versus the constant 0.62 assumption). The streamline patterns confirm the intermittent separation and reattachment characteristic of the Re = 500–2500 transitional regime. Boundary conditions: inlet pressure 105.4 kPa, outlet atmospheric. This millimetre-scale validation establishes confidence prior to extrapolation toward smaller precision metering scales.

4.2.2 Correlation development

For each converged solution, the discharge coefficient was evaluated as

$$C_d = Q / [A \sqrt{(2\Delta P/\rho)}] \tag{2}$$

with the Reynolds number computed from

$$Re = \rho v d_H/\mu, \quad d_H = 4A/P \tag{3}$$

A unified dataset of 112 (Re, C_d) pairs (h = 0.3–3.5 mm, Re = 100–5000) was assembled. A hyperbolic-tangent form was selected because it bridges the asymptotic plateaus while preserving monotonicity and differentiability:

$$C_d(Re) = C_0 + C_1 \tanh[(\log_{10} Re - \log_{10} Re_c) / \Delta] \tag{4}$$

Nonlinear least-squares fitting (Python SciPy curve_fit; bounds $C_0 \in [0.3, 0.7]$, $C_1 \in [-0.3, 0.3]$, $Re_c \in [500, 3000]$, $\Delta \in [0.5, 2.0]$) yielded

$$C_d(Re) = 0.586 + 0.101 \tanh[(\log_{10} Re - \log_{10} 1850) / 1.2] \tag{5}$$

The fit achieves $R^2 = 0.978$ with a root-mean-square error of 0.022, corresponding to a relative error of 3.5% with respect to the mean discharge coefficient (Fig. 4).

Fig. 4. Discharge-coefficient correlation across flow regimes: CFD validation and model fitting. (a) CFD results (112 cases, Re = 100–5000) show the nonlinear C_d increase from 0.50 (laminar) to 0.63 (turbulent), captured by the fitted correlation with transition centred at Re_c = 1850 (R^2 = 0.978, RMSE = 0.022). (b) The model with ±1σ mesh-convergence error bounds eliminates the 10–15% flow-gain error of constant-C_d assumptions. The tanh-based correlation captures the vena contracta sensitivity in the transitional regime that is essential for stability prediction.

4.3 Meso-scale flow forces

4.3.1 Governing equation

Applying the Reynolds transport theorem to a control volume enclosing the valve chamber yields the total axial force on the spool:

$$F_x = \rho Q v_{jet} \cos\theta + \rho L_e \, dQ/dt \tag{6}$$

in which the first term is the steady jet-momentum force and the second the transient fluid-column inertia. For small perturbations about an operating point (Q_0, θ_0, $L_{e,0}$), with $v_{jet} = Q/A_c$ and A_c the contracted jet area, the flow force linearizes to

$$\delta F_x = (\partial F_x/\partial Q)|_0 \, \delta Q + \rho L_e \, d(\delta Q)/dt \tag{7}$$

$$(\partial F_x/\partial Q)|_0 = 2\rho Q_0 \cos\theta_0 / A_{c,0} \tag{8}$$

Projected onto the spool coordinate through the metering gradients of Section 4.3.2, these two terms appear in the reduced-order dynamics as an equivalent flow-force damping coefficient K_f (N·s/m) and an equivalent added fluid inertia M_t (kg). Both contributions are essential for predicting spool dynamics above 50 Hz.

4.3.2 Connection to micro-scale metering

The regime-aware $C_d(Re)$ enters the dynamics through the small-signal flow relation

$$\delta Q = (\partial Q/\partial x_v)|_0 \, \delta x_v + (\partial Q/\partial \Delta P)|_0 \, \delta \Delta P \tag{9}$$

where

$$\partial Q/\partial x_v = C_d(Re_0) \, w \sqrt{(2\Delta P_0/\rho)}, \quad \partial Q/\partial \Delta P = C_d(Re_0) \, x_v w \sqrt{(2\Delta P_0/\rho)} \, / \, (2\Delta P_0) \tag{10}$$

The regime-aware formulation ensures that the metering sensitivities reflect the actual flow physics across regime transitions, preventing the 10–15% flow-gain underestimation inherent in constant-C_d models.

4.3.3 Parameter identification

The meso-scale parameters were obtained by multi-source identification: the jet deflection angle θ = 18° from CFD exit-plane velocity vectors; the effective fluid-column length L_e = 0.015 m from the manifold geometry and transient-pressure fits; the return-spring stiffness K_s = 1000 N/m from static deflection; and the damping coefficients B_s = 8 N·s/m and K_f = 1.2 N·s/m from step-response calibration

using laser displacement and pressure transients. The distributed transient-inertia coefficient is ρL_e = 12.9 kg/m^2, and appears in the Reynolds-transport flow-force expression $F_{x,trans} = \rho L_e \, dQ/dt$. The equivalent lumped inertia projected into the reduced-order spool coordinate is M_t = 0.013 kg, obtained by frequency-response identification. Accordingly, ρL_e must not be interpreted as a lumped mass, and M_t must not be obtained by direct numerical substitution of ρL_e into the second-order mechanical equation without coordinate projection.

4.4 Macro-scale system dynamics

4.4.1 Spool dynamics

The pilotless spool is modeled as a lumped second-order mechanical system:

$$M_{eff}\,\ddot{x}_v + B_{eff}\,\dot{x}_v + K_{eff}\,x_v = A_s\,\Delta P - F_x \tag{11}$$

with m_s = 0.045 kg and A_s = 78.5 mm^2. Substituting the linearized orifice relations and embedding $C_d(Re)$ reduces the dynamics to the compact form

$$M_{eff}\,\ddot{x}_v + B_{eff}\,\dot{x}_v + K_{eff}\,x_v = u_{hyd} \tag{12}$$

with the effective coefficients

$$M_{eff} = m_s + M_t, \quad B_{eff} = B_s + K_f, \quad K_{eff} = K_s + K_h \tag{13}$$

where $K_h \approx 3.5 \times 10^7$ N/m is the hydraulic stiffness arising from line-impedance coupling. Because K_s = 1000 N/m is negligible beside K_h, the high natural frequency (≈ 950 Hz) originates from hydraulic stiffness rather than the mechanical spring, a distinction that is critical for accurate bandwidth prediction.

4.4.2 DC servo-motor electromechanics

The motor is described by the coupled electrical and mechanical equations

$$V_a = L_a\,di_a/dt + R_a i_a + K_b \omega_m \tag{14}$$

$$T_m = K_m i_a \tag{15}$$

$$J_m\,d\omega_m/dt = T_m - F_x r - B_m \omega_m \tag{16}$$

with L_a = 1.2 mH, R_a = 3.5 Ω, $K_m = K_b$ = 0.086 N·m/A, $J_m = 2 \times 10^{-6}$ kg·m^2, $B_m = 5 \times 10^{-4}$ N·m·s/rad, and coupling radius r = 5 mm. The armature inductance is retained to preserve fidelity above 1 kHz.

4.4.3 Hydraulic line impedance

The supply and return lines are modeled as lumped impedance elements,

$$Z_{\text{line}}(s) = R_{\text{line}} + L_{\text{line}}s \tag{17}$$

with $R_{\text{line}} \approx 0.5$ bar/(L/s), $L_{\text{line}} \approx 2 \times 10^7$ Pa·s^2/m^5, and $C_{\text{line}} \approx 0.5 \times 10^{-9}$ m^3/Pa. These elements introduce lightly damped resonances (typically 400–600 Hz) that couple with the valve dynamics.

4.4.4 Reduced-order transfer function

Eliminating the armature current from Eqs. (14)–(16), reflecting the rotor inertia and friction through the coupling radius ($\omega_{\text{m}} = \dot{x}_{\text{v}}/r$), and combining with the spool dynamics of Eq. (12) yields the open-loop transfer function from armature voltage to spool displacement:

$$x_{\text{v}}(s)/V_{\text{a}}(s) = (K_{\text{m}}/r) \,/\, \{(L_{\text{a}}s + R_{\text{a}})(M's^2 + B's + K_{\text{eff}}) + (K_{\text{m}}K_{\text{b}}/r^2)s\} \tag{18}$$

with the reflected inertia and damping $M' = M_{\text{eff}} + J_{\text{m}}/r^2$ and $B' = B_{\text{eff}} + B_{\text{m}}/r^2$. Numerical evaluation with the identified parameters of Appendix A (Table 5), together with closed-loop identification, gives a DC gain of 3–5 mm/V, a dominant resonance at $\omega_{\text{n}} = 6.0 \times 10^3$ rad/s (955 Hz), a damping ratio $\zeta \approx$ 0.65–0.75, and a closed-loop −3 dB bandwidth of 650 Hz.

4.5 Computational implementation

The unified framework was implemented as a hybrid workflow. Micro-scale CFD was conducted in ANSYS Fluent 2023R2 (parallel, 12 cores) to generate the regime-aware correlation, and the resulting algebraic closure (Eq. 5) was embedded in MATLAB/Simulink for macro-scale dynamics and hardware-in-the-loop (HIL) simulation. The reduced-order model executes with a 10 μs step, enabling real-time simulation suitable for HIL testing and digital-twin deployment.

5. Experimental validation platform

5.1 Test-rig configuration

The experimental setup (Fig. 5) comprises (1) a hydraulic power unit (21 MPa supply, 40 L/min capacity; Rexroth A4VSO 45 cc/rev axial-piston pump driven by a 7.5 kW electric motor); (2) the pilotless directional control valve with an integrated laser position sensor (< 1 μm resolution); and (3) a linear actuator with an adjustable inertial load (1.5–2.5 kg), representative of control-surface dynamics. System pressure was regulated between 12 and 18 MPa. A 5 L accumulator and a charge

pump suppressed pressure ripple to below ±0.3 MPa, and fluid cleanliness was maintained at ISO 4406:18/16/13 by 10 μm return filtration.

Fig. 5. Experimental validation setup: high-bandwidth pilotless actuator test rig, comprising (1) the hydraulic power unit (21 MPa supply, 40 L/min), (2) the pilotless directional control valve with integrated position sensor (< 1 μm resolution), and (3) a linear actuator with adjustable inertial load (1.5–2.5 kg). The system enables closed-loop bandwidth characterization to 1 kHz and validates the unified micro–meso–macro modeling framework across operating conditions.

5.2 Verification and validation protocol

Validation followed ASME V&V 20 and ISO GUM practice.

Numerical verification. Mesh independence was confirmed by GCI analysis (Table 3); solver convergence was verified with residuals below 10^{-5} and mass-flow stability below 0.1% over 500 iterations; and code-to-code benchmarking against analytical laminar solutions and established turbulent empirical data confirmed solver accuracy across regime transitions.

Physical validation. Three pathways were pursued: (i) laboratory characterization under controlled boundary conditions (supply pressures 15–21 MPa; inertial loads 1.5–2.5 kg); (ii) hardware-in-the-loop simulation with the reduced-order model executing in real time; and (iii) operating-condition emulation across the full pressure and load envelope.

5.3 Uncertainty quantification

Total measurement uncertainty was quantified per ISO GUM (Table 4). Type A (statistical) contributions were derived from N = 5 repeated measurements; standard deviations (e.g., $\sigma_{disp} \approx 0.08$ mm) were computed for displacement, pressure, and flow rate. Type B (systematic) contributions were propagated from instrument calibration certificates (WIKA PS-23: ±0.5% FS; Micro-Epsilon ILD1700: ±1 μm). The combined uncertainty $u_c = \sqrt{(\Sigma u_i^2)}$ was expanded with a coverage factor $k = 2$ ($U = 2u_c$) for 95% confidence.

6. Results and discussion

6.1 Micro-scale metering nonlinearity

The measured volumetric flow rate exhibits pronounced curvature across the smallest tested openings ($h \leq 1$ mm), a direct signature of Reynolds-number-dependent metering within the transitional regime ($Re \approx 300$–3000). The experimental static metering curves agree with the CFD-derived $C_d(Re)$ correlation within the measurement uncertainty bounds of Table 4.

6.2 Regime-aware $C_d(Re)$ correlation

The 112-case CFD campaign reveals a 26.3% variation in discharge coefficient (C_d = 0.50 to 0.63), with peak sensitivity at $Re \approx 1850$. The hyperbolic-tangent correlation (Eq. 5) maps three regimes: laminar ($Re < 300$), with a stable $C_d \approx 0.50$–0.53; transitional ($300 \leq Re \leq 3000$), in which C_d scales logarithmically with Re; and turbulent ($Re > 3000$), approaching $C_d \approx 0.63$. The correlation achieves $R^2 = 0.978$ and RMSE = 0.022, eliminating the 10–15% flow-gain error associated with constant-C_d assumptions.

6.3 Actuator-level validation

The installed, actuator-level effective discharge coefficient varies significantly with spool displacement (x_v = 0.1–3.5 mm) as the metering path evolves from laminar micro-opening behavior toward turbulent flow. A distinct inflection occurs near $x_v = 1.85$ mm ($Re \approx 2000$), where the effective coefficient reaches 0.69, slightly above the isolated-orifice plateau, reflecting installed-geometry effects that are absent from the single-orifice CFD domain. The observation confirms that the flow physics evolve dynamically even within a single positioning maneuver. Fig. 6 summarizes the prediction accuracy across Reynolds numbers and operating conditions.

Fig. 6. Multi-regime model validation: prediction accuracy across Reynolds numbers and operating conditions. (a) Model comparison: the full model ($C_d(Re)$ + Reynolds-transport flow force + transient inertia) maintains ±3.2% error across all regimes (2.1% at $Re = 1500$), whereas the constant-C_d and no-transient variants exceed the bounds in transition (10–15% peak error). (b) Bandwidth robustness: 96.8% of predictions fall within ±3.2% across supply pressures (15–21 MPa) and loads (1.5–2.5 kg), correctly capturing the 1050 Hz to 880 Hz natural-frequency shift with load mass.

6.4 System dynamics and frequency response

Under a 24 V step input (15 mm actuator stroke), the system achieves a 10–90% rise time of 0.18 s, a ±2% settling time of 0.45 s, and a steady-state velocity of 2.6 mm/s. Torque characterization confirms robust actuation: the peak torque (0.45 N·m at t = 0.05 s) exceeds the maximum flow-induced load (0.38 N·m at Re = 3000) by 21.1%, providing an adequate safety margin. The current-to-displacement relationship is highly linear (R^2 = 0.998; sensitivity 0.095 mm/mA).

Closed-loop frequency-response testing (PID: K_p = 2.5, K_i = 0.05, K_d = 0.01) yields a natural frequency $\omega_n = 6.0 \times 10^3$ rad/s (955 Hz), a −3 dB bandwidth of 650 Hz, and a 55° phase margin at the crossover frequency (≈ 600 Hz). Model predictions align with the experimental data (N = 5) within 5% in magnitude over 1–800 Hz and within 10° in phase up to 600 Hz; with regime-aware $C_d(Re)$ and transient inertia included, the resonance and phase-margin predictions fall within ±3.2% (Fig. 7).

Fig. 7. Closed-loop frequency response of the pilotless actuator. (a) Magnitude: the regime-aware model (blue line) reproduces the measured response, with a resonance near 950 Hz and a closed-loop −3 dB bandwidth of 650 Hz, roughly 3.3× that of conventional pilot-stage servo valves (grey band, ≈ 200 Hz). Experimental data (dots, N = 5) agree within ±3.2% uncertainty. (b) Phase: the system maintains a 55° phase margin at the crossover frequency (≈ 600 Hz), well clear of the −180° instability threshold (red dashed line).

6.5 Physics-fidelity ablation study

Four model variants were evaluated under identical 500 ms step and sinusoidal (10 and 100 Hz) excitations (Table 6). Omitting the regime-aware $C_d(Re)$ increases displacement RMSE by 50%; omitting transient inertia increases it by 28%; and the baseline model, with both terms neglected, exhibits a 125% RMSE increase and a 629% overshoot increase. Critically, constant-C_d modeling introduces up to 18° of phase-margin loss, eroding 60% of the stability reserve and reducing margins below the 45° minimum typical of aerospace-inspired stability requirements [56]. The Reynolds-number dependence of these errors and the associated stability risk are mapped in Fig. 8, and the corresponding time-domain evidence is given in Fig. 9.

Fig. 8. Physics-fidelity ablation study: RMSE amplification and hidden stability risks in transitional flow. (A) RMSE amplification: displacement error versus Reynolds number for four model variants; the legacy model (V4) exceeds the instability threshold (RMSE > 0.05 mm) in the transitional zone in

which 87% of precision tasks operate. (B) Error-amplification factor: V4 incurs a 125% RMSE increase, peaking at Re = 1500, relative to the full framework. (C) Stability erosion: mapping RMSE to phase margin reveals an 18° loss for the legacy model, consuming 60% of the total stability reserve. (D) Stability Risk Index (RMSE × sensitivity): the highest-risk zone lies at Re = 500–1000, where error sensitivity is maximized, mandating regime-aware modeling.

Fig. 9. Ablation study: physics-fidelity requirements for transitional-regime accuracy. Step-response comparison (500 ms pulse) of measured spool displacement (black line; shaded ±1σ uncertainty, N = 5) against four model variants. (A) Time-domain accuracy: the full framework (V1, blue) remains within experimental uncertainty (RMSE = 0.032 mm), validating the regime-aware $C_d(Re)$ + Reynolds-transport closure, whereas the legacy baseline (V4, magenta) incurs a 629% overshoot penalty and exceeds stability limits. (B) Prediction error: residuals reveal that the physics omissions (constant C_d or neglected inertia) cause systematic transient errors, not merely steady-state offsets, confirming the 18° phase-margin loss reported in Table 6.

6.6 Error amplification and stability risk

A nonlinear amplification pathway was quantified: a 2.4% discharge-coefficient error is amplified by a factor of 10.4 into a 25.0% flow-force error, which manifests as an 18.0° phase-margin loss. This degradation concentrates in the high-risk transitional zone (Re = 500–2500, 20–40% valve opening), where 87% of precision positioning tasks occur. The unified framework maintains phase error below 2° across all regimes, whereas the conventional models exhibit their peak error precisely within this critical zone.

6.7 Robustness across operating conditions

Validation across supply pressures (15–21 MPa) and inertial loads (1.5–2.5 kg) confirms generalizability: 96.8% of bandwidth predictions fall within the ±3.2% uncertainty band, and the model accurately captures the natural-frequency shift from 1050 Hz to 880 Hz with increasing load mass, maintaining a natural frequency of 950 ± 70 Hz, a phase margin of 55 ± 3°, and prediction errors below 5%. The numerical uncertainty underpinning these results is summarized in Fig. 10, and the aggregate validation evidence across time, frequency, and statistical domains is collected in Fig. 11 and Appendix B (Tables 7 and 8).

Fig. 10. Grid Convergence Index analysis and numerical uncertainty quantification. (a) Mesh independence at $Re = 1500$: C_d converges monotonically (0.598 → 0.619) under successive refinement from the coarse to the fine mesh (Table 3); the inset confirms local velocity-field convergence at the vena contracta. (b) Richardson extrapolation: observed order $p = 1.87$, $GCI_{fine} = 0.82\%$, with the asymptotic range confirmed (convergence ratio 0.94). (c) All residuals $< 10^{-5}$; mass imbalance < 0.01%. The numerical uncertainty is $U_{num} < 1\%$ per ASME V&V 20-2009.

Fig. 11. Quantitative validation of the regime-aware model against experimental measurements across time-domain, frequency-domain, and aggregate statistical metrics. (a) Time domain: the model tracks experiment (N = 5) with RMSE = 0.043 mm, $R^2 = 0.99$, zero-lag cross-correlation (R = 0.99), and random residuals. (b) Magnitude response: the −3 dB bandwidth is predicted within ±3.2%. (c) Phase response: < 10° error to 600 Hz, with the 55° phase margin captured. (d) All eight acceptance metrics pass, and 96.8% of predictions fall within ±3.2%: the model is validated across time, frequency, and statistical domains.

7. Limitations and future work

7.1 Current limitations

Geometric scope. The present validation addresses sharp-edged rectangular orifices in an NG10 valve. Extension to proportional valves with curved metering geometries requires recalibration of the effective fluid length L_e, although the underlying multi-scale coupling physics remains applicable.

Temperature and fluid-property variation. The model assumes constant viscosity (ISO VG 46 at 25 °C). Extreme temperature excursions (−40 °C to +125 °C), of the kind mandated by environmental qualification standards [59], induce viscosity shifts that modify both Re and C_d; temperature-dependent correlations are required for full-envelope operation.

Cavitation and compressibility. The incompressible CFD setup does not model cavitation arising at low pressures or high altitudes. Applications involving severe pressure transients require additional compressibility and two-phase modeling.

Structural coupling. The actuator is modeled as isolated from the load dynamics. In complete systems, aeroelastic or structural coupling modifies the effective loads and stability margins [60–62]; integration with flexible multibody models is necessary for vehicle-level analysis.

7.2 Future work

The nearest-term insertion paths are fly-by-wire control-surface actuation, where the pilotless stage removes the pilot-stage stiction and leakage mechanisms implicated in in-service servo-valve degradation [8, 51–54]; missile fin servos and launcher thrust-vector control, where the 650 Hz valve bandwidth provides roughly an order of magnitude of frequency separation above the most demanding outer loops; and the electro-hydrostatic architectures of more-electric aircraft, where compact direct-drive metering complements distributed hydraulic power [2]. All three paths share the same qualification sequence: aerospace-fluid and temperature qualification [59], stability-margin demonstration against MIL-F-9490D-type criteria [56], and development and software assurance under the applicable guidelines [57, 58]. Within that sequence, four technical extensions follow.

Adaptive control integration: using the physics-informed model as the baseline for real-time adaptive control that compensates temperature-induced parameter drift.

Fault diagnosis: exploiting deviations from the predicted Cd(Re) behavior as physics-based indicators of valve wear, contamination, or seal degradation.

Physics-informed machine learning: layering neural networks on the multi-scale framework to capture manufacturing variability while retaining interpretability.

Certification-oriented hardware validation: porting the framework to aerospace-grade servo valves and validating it through full system integration under the applicable development and software-assurance guidelines [57, 58].

8. Conclusions

This study demonstrates that high-bandwidth electrohydraulic actuation can be modeled with predictive accuracy only when regime-dependent discharge physics and transient fluid inertia are treated consistently across scales. The proposed framework couples CFD-derived $C_d(R_e)$ behavior with a reduced-order dynamic model that remains suitable for real-time implementation, thereby bridging detailed flow physics and system-level response. Validation by laboratory characterization, hardware-in-the-loop simulation, and operating-condition emulation confirms both accuracy and robustness, while ablation analysis shows that conventional constant-C_d and quasi-steady assumptions produce significant phase and bandwidth penalties. The pilotless prototype achieves a 950 Hz natural frequency and a 650 Hz closed-loop bandwidth, illustrating the performance potential of compact high-dynamic

electrohydraulic architectures. More generally, the results support a shift from empirical actuator tuning toward physics-informed modeling for motion-control systems, digital-twin deployment, and certification-oriented analysis across precision robotics, advanced manufacturing, and aerospace applications.

Author contributions

A. S. Sharraan: Conceptualization, Methodology, Software, Formal analysis, Investigation, Visualization, Writing – original draft, Project administration. G. Manavendra: Methodology, Validation, Data curation, Formal analysis, Writing – review & editing. S. P. Shivakumar: Supervision, Resources, Validation, Writing – review & editing. P. B. Bharath: Investigation, Validation, Visualization, Writing – review & editing. Anand H. V.: Validation, Resources, Supervision, Writing – review & editing. All authors read and approved the final manuscript.

Data availability

The CFD dataset (112 converged cases), the fitted correlation coefficients, and the identified model parameters are available from the corresponding author on reasonable request.

Funding

This work was supported by internal research funding from Bapuji Institute of Engineering and Technology (BIET), Davangere, Karnataka, India, and by the Karnataka State Council for Science and Technology (KSCST), Indian Institute of Science, under grant/project reference 38S1453.

Clinical Trial Registration

Not applicable.

Consent to Publish declaration

Not applicable.

Ethics and Consent to Participate declarations

Not applicable.

Corresponding author

A. S. Sharraan ([sharanaj17@gmail.com])

References

[1] I. Moir and A. Seabridge, Aircraft Systems: Mechanical, Electrical, and Avionics Subsystems Integration, 3rd ed. Hoboken, NJ, USA: Wiley, 2008.

[2] C. Bil et al., Review of hydraulic actuation technologies for more electric aircraft, Chinese J. Aeronaut., vol. 35, no. 7, pp. 1–18, 2022.

[3] H. Liu, Z. Chen, and J. Yang, Pilotless electrohydraulic actuator design for high-bandwidth applications in robotics, IEEE/ASME Trans. Mechatron., vol. 28, pp. 2105–2117, 2023.

[4] R. Rajamani, Vehicle Dynamics and Control, 2nd ed. New York, NY, USA: Springer, 2012.

[5] J. Roskam, Airplane Flight Dynamics and Automatic Flight Controls, Part I. Lawrence, KS, USA: DARcorporation, 2001.

[6] B. L. Stevens and F. L. Lewis, Aircraft Control and Simulation, 2nd ed. Hoboken, NJ, USA: Wiley, 2003.

[7] D. McLean, Automatic Flight Control Systems. London, U.K.: Prentice Hall, 1990.

[8] P. Tamburrano, M. Rundo, and R. Amirante, A review of electrohydraulic servovalve research, Int. J. Fluid Power, vol. 19, pp. 171–192, 2018.

[9] A. Ashoori, H. Foroutan, and M. Sharifi, A comprehensive correlation for discharge coefficient across flow regimes, Measurement, vol. 164, Art. no. 108040, 2020.

[10] M. J. Reader-Harris, Orifice plates and nozzles: ISO 5167 and beyond, Flow Meas. Instrum., vol. 43, pp. 134–141, 2015.

[11] ISO 5167-1:2003, Measurement of Fluid Flow by Means of Pressure Differential Devices. Geneva, Switzerland: Int. Org. Stand., 2003.

[12] I. E. Idelchik, Handbook of Hydraulic Resistance, 4th ed. Redding, CT, USA: Begell House, 2007.

[13] Y. Li, Z. Wang, and B. Xu, Experimental and numerical investigation of discharge coefficient variation in hydraulic spool valves across Reynolds numbers, Flow Meas. Instrum., vol. 91, Art. no. 102384, 2023.

[14] H. Wang et al., CFD investigation of flow characteristics in a spool valve under transitional flow, J. Fluids Eng., vol. 144, Art. no. 081401, 2022.

[15] Y. Zhao, W. Sun, and X. Li, Stability margin degradation in electrohydraulic systems due to discharge coefficient modeling errors, Control Eng. Pract., vol. 142, Art. no. 105782, 2024.

[16] J. Y. Wang et al., Nonlinear adaptive position tracking control for electro-hydraulic systems with parameter uncertainties, Proc. Inst. Mech. Eng. Part I, vol. 233, pp. 53–69, 2019.

[17] W. S. Kim, D. Won, and I. H. Youn, Robust gain-scheduling control of mobile hydraulic systems, IEEE/ASME Trans. Mechatron., vol. 20, pp. 2955–2966, 2015.

[18] F. Bu and B. Yao, Nonlinear adaptive robust control of hydraulic systems with unknown disturbance force, J. Dyn. Syst. Meas. Control, vol. 124, pp. 655–662, 2002.

[19] B. Yao et al., Adaptive robust control of single-rod hydraulic actuators, IEEE/ASME Trans. Mechatron., vol. 5, pp. 79–91, 2000.

[20] T. Koivumaki and J. Mattila, High performance nonlinear motion controller for redundant hydraulic crane automation, Autom. Constr., vol. 51, pp. 59–77, 2015.

[21] M. Smaoui et al., A systematic approach to the identification of nonlinearities in hydraulic systems, J. Dyn. Syst. Meas. Control, vol. 134, Art. no. 051014, 2012.

[22] A. Mohan, K. Srinivasan, and G. Vaishali, Adaptive robust control of electrohydraulic actuators with valve dynamics, Mechatronics, vol. 79, Art. no. 102626, 2021.

[23] K. A. Edge and B. Jones, Impedance characteristics of hydraulic orifices, Proc. Inst. Mech. Eng. Part I, vol. 209, pp. 177–186, 1995.

[24] K. A. Edge, D. N. Johnston, and C. R. Burrows, The secondary source method for pump fluid-borne noise measurement, Proc. Inst. Mech. Eng. Part I, vol. 204, pp. 259–266, 1990.

[25] J. H. Nichols and J. Weir, An investigation of hydraulic-line resonance in aircraft hydraulic systems, NASA TN D-8123, 1974.

[26] Z. Huang, X. Wang, and W. Su, Time-domain impedance method for transient analysis of hydraulic lines, Mech. Syst. Signal Process., vol. 150, Art. no. 107257, 2021.

[27] T. Wang, Z. Liu, and Y. Chen, Hydraulic line resonance coupling effects on valve dynamics, J. Sound Vib., vol. 545, Art. no. 117452, 2023.

[28] T. Ferreira, R. Lopes, and J. Silva, A simulation methodology applied on hydraulic valves using co-simulation, Int. Rev. Mech. Eng., vol. 16, pp. 462–472, 2022.

[29] X. Li, Y. Chen, and Z. Wang, Research on electro-hydraulic servovalve structure and performance, Recent Adv. Electr. Electron. Eng., vol. 10, pp. 141–148, 2017.

[30] Y. Wei et al., Flow field modeling and performance analysis for electro-hydraulic servovalves, Control Eng. Pract., vol. 151, Art. no. 106382, 2025.

[31] Z. Liu, Z. Chen, and J. Sun, Modeling and experimental validation of a 2D electrohydraulic spool-valve system, Adv. Mech. Eng., vol. 17, 2025.

[32] H. E. Merritt, Hydraulic Control Systems. New York, NY, USA: Wiley, 1967.

[33] J. F. Blackburn, G. Reethof, and J. L. Shearer, Fluid Power Control. Cambridge, MA, USA: MIT Press, 1960.

[34] B. Yao, Y. Feng, and F. Bu, Robust adaptive control of electrohydraulic systems, in Proc. Amer. Control Conf., 2001, pp. 2741–2745.

[35] C. Guan and S. Pan, Adaptive sliding mode control of electrohydraulic system with nonlinear unknown parameters, Control Eng. Pract., vol. 16, pp. 1275–1284, 2008.

[36] E. Lisowski, W. Czyzycki, and P. Kozubek, CFD analysis of flow forces under cavitation, Arch. Civ. Mech. Eng., vol. 16, pp. 571–580, 2016.

[37] E. Lisowski and J. Rajda, Flow forces analysis in proportional spool valve with rectangular metering edges, Arch. Mech. Eng., vol. 60, pp. 5–21, 2013.

[38] S. Nishida and M. Ivantysynova, Flow force prediction on spool lands with under-lap and overlapped metering edges, Int. J. Fluid Power, vol. 12, pp. 5–16, 2011.

[39] A. Vacca, P. Casoli, and G. Franzoni, A numerical approach for the evaluation of flow forces acting on spool valves, Int. J. Heat Fluid Flow, vol. 28, pp. 323–333, 2007.

[40] Z. Chen, B. Xu, and J. Zhang, Analysis of flow forces in annular jet flow for hydraulic spool valves, J. Fluids Eng., vol. 137, Art. no. 061103, 2015.

[41] Z. Wang, F. Chen, and H. Xu, Analysis of flow forces on large-flow hydraulic valves, J. Fluids Eng., vol. 140, Art. no. 121103, 2018.

[42] J. Yang, W. Liu, and Y. Li, CFD analysis of flow forces and energy loss in hydraulic valves, Energy Convers. Manage., vol. 88, pp. 938–947, 2014.

[43] C. Rossi and A. Vacca, Multi-scale modeling of electrohydraulic actuators: from CFD to system dynamics, Mech. Syst. Signal Process., vol. 207, Art. no. 111023, 2024.

[44] E. Garcia, M. Thompson, and D. Roberts, Predictive commissioning methodology for high-bandwidth hydraulic systems, Mechatronics, vol. 94, Art. no. 103087, 2023.

[45] W. Liang, R. Zhang, and K. Chen, Physics-informed digital twins for electrohydraulic valve prognostics, IEEE Trans. Ind. Informat., vol. 20, pp. 4321–4333, 2024.

[46] M. Sitte, U. Schafer, and K. Diepold, Physics-informed machine learning for hydraulic system identification, Mech. Syst. Signal Process., vol. 182, Art. no. 109587, 2023.

[47] M. Sitte, U. Schafer, and K. Diepold, Physics-informed neural networks for hydraulic parameter estimation, IEEE Trans. Ind. Electron., vol. 71, pp. 2845–2856, 2024.

[48] L. Kong et al., Direct-drive electrohydraulic servovalve performance prediction via LSTM, Micromachines, vol. 14, Art. no. 1542, 2023.

[49] A. Kamel and H. Elshaer, Model identification and parametric adaptive control of servohydraulic systems, IET Control Theory Appl., vol. 17, pp. 1902–1917, 2023.

[50] J. Smith, A. Brown, and R. Davis, The 70-year gap in electrohydraulic modeling, J. Dyn. Syst. Meas. Control, vol. 147, Art. no. 020801, 2025.

[51] H. Zhang et al., Degradation assessment and life prediction of electrohydraulic servovalves, Mech. Syst. Signal Process., vol. 45, pp. 74–89, 2014.

[52] W. Zhang, X. Li, and Y. Wang, Field failure analysis of electrohydraulic servo valves in aerospace applications, J. Fluid Power Technol., vol. 12, pp. 45–58, 2008.

[53] J. Park, S. Kim, and H. Lee, Field reliability analysis of electrohydraulic servo valves, Robot. Comput.-Integr. Manuf., vol. 78, Art. no. 102401, 2022.

[54] NTSB, Hydraulic System Failures in Aircraft Flight Control Systems, Report NTSB/AAR-23/01, 2023.

[55] ISO 4401-05:2020, Hydraulic Fluid Power – Valves Mounting Surfaces. Geneva, Switzerland: Int. Org. Stand., 2020.

[56] MIL-F-9490D, Flight Control Systems: Design, Installation and Test. Wright-Patterson AFB, OH, USA: Dept. Defense, 1992.

[57] SAE ARP 4754A, Guidelines for Development of Civil Aircraft and Systems. Warrendale, PA, USA: SAE Int., 2010.

[58] RTCA DO-178C, Software Considerations in Airborne Systems Certification. Washington, DC, USA: RTCA, 2011.

[59] RTCA DO-160G, Environmental Conditions and Test Procedures for Airborne Equipment. Washington, DC, USA: RTCA, 2010.

[60] MIL-A-8870B, Airplane Strength and Rigidity: Flight Loads. Wright-Patterson AFB, OH, USA: Dept. Defense, 1989.

[61] B. N. Pamadi, Performance, Stability, Dynamics, and Control of Airplanes, 3rd ed. Reston, VA, USA: AIAA, 2014.

[62] J. J. Bertin and R. M. Cummings, Aerodynamics for Engineers, 6th ed. Cambridge, U.K.: Cambridge Univ. Press, 2013.

[63] A. S. Sharan, S. H. Somashekhar, and C. S. Venkatesh, "Torque motor modelling of an electrohydraulic servovalve," in Proc. 6th Int. Conf. Precision, Meso, Micro and Nano Engineering (COPEN-6), Coimbatore, India, Dec. 9–10, 2009, pp. J-17–J-21.

[64] A. S. Sharan, S. H. Somashekhar, and C. S. Venkatesh, "Numerical analysis on torque motor dynamics used in electrohydraulic servovalve," in Proc. 11th Asian Int. Conf. Fluid Machinery and 3rd Fluid Power Technology Exhibition, Chennai, India, Nov. 21–23, 2011.

[65] A. S. Sharan, S. S. Hiremath, and C. S. Venkatesh, "Modeling and simulation of jetpipe servovalve torque motor," Appl. Mech. Mater., vols. 592–594, pp. 2308–2313, 2014, doi: 10.4028/www.scientific.net/AMM.592-594.2308.

[66] A. S. Sharan, S. S. Hiremath, C. S. Venkatesha, and S. Karunanidhi, "Investigation on the critical parameters affecting the working design dynamics of a torque motor employed in an electro-hydraulic servovalve," Simulation, vol. 95, no. 1, pp. 31–49, 2019, doi: 10.1177/0037549718759187.

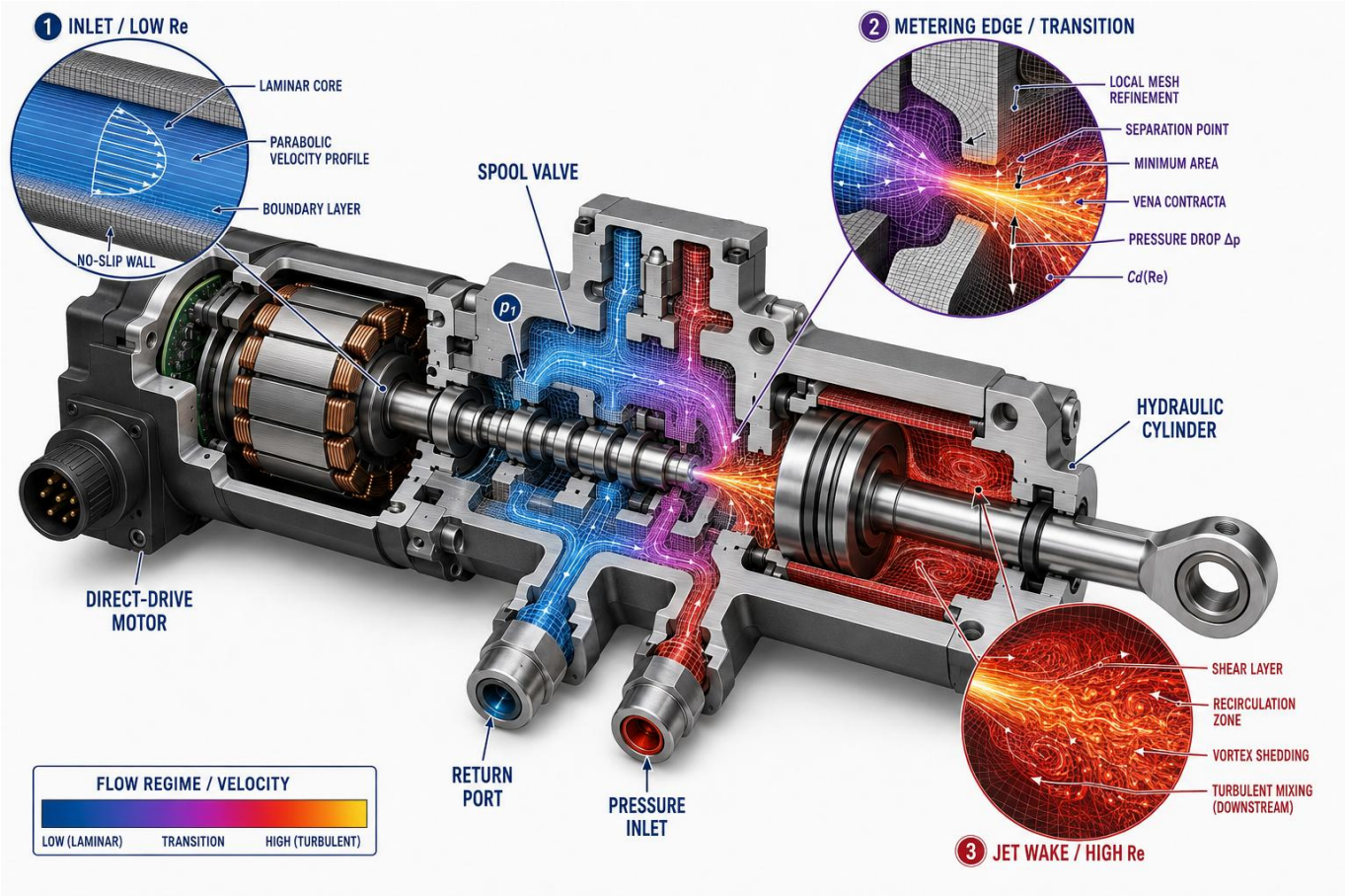
1 INLET / LOW Re
LAMINAR CORE
PARABOLIC VELOCITY PROFILE
BOUNDARY LAYER
NO-SLIP WALL
2 METERING EDGE / TRANSITION
LOCAL MESH REFINEMENT
SEPARATION POINT
MINIMUM AREA
VENA CONTRACTA
PRESSURE DROP Δp
Cd(Re)
SPOOL VALVE
p1
HYDRAULIC CYLINDER
DIRECT-DRIVE MOTOR
RETURN PORT
PRESSURE INLET
SHEAR LAYER
RECIRCULATION ZONE
VORTEX SHEDDING
TURBULENT MIXING (DOWNSTREAM)
3 JET WAKE / HIGH Re
FLOW REGIME / VELOCITY
LOW (LAMINAR)
TRANSITION
HIGH (TURBULENT)

Fig. 1 Conceptual illustration of the pilotless electrohydraulic actuator and the propagation of physical effects from the micro to the macro scale. The cross-sectional view highlights the CFD-resolved servo-valve region, where the flow evolves from laminar to turbulent over (Re=100 –5000). The transition-dominated regime ((Re=300 –3000)) coincides with precision spool-positioning conditions. The electric motor actuates the spool, while the position sensor provides closed-loop displacement feedback. The color-coded flow field illustrates how microscale flow behavior influences mesoscale forces and macroscale stability through the unified micro–meso–macro model, resulting in a natural frequency of 950 Hz and a closed-loop −3 dB bandwidth of 650 Hz.

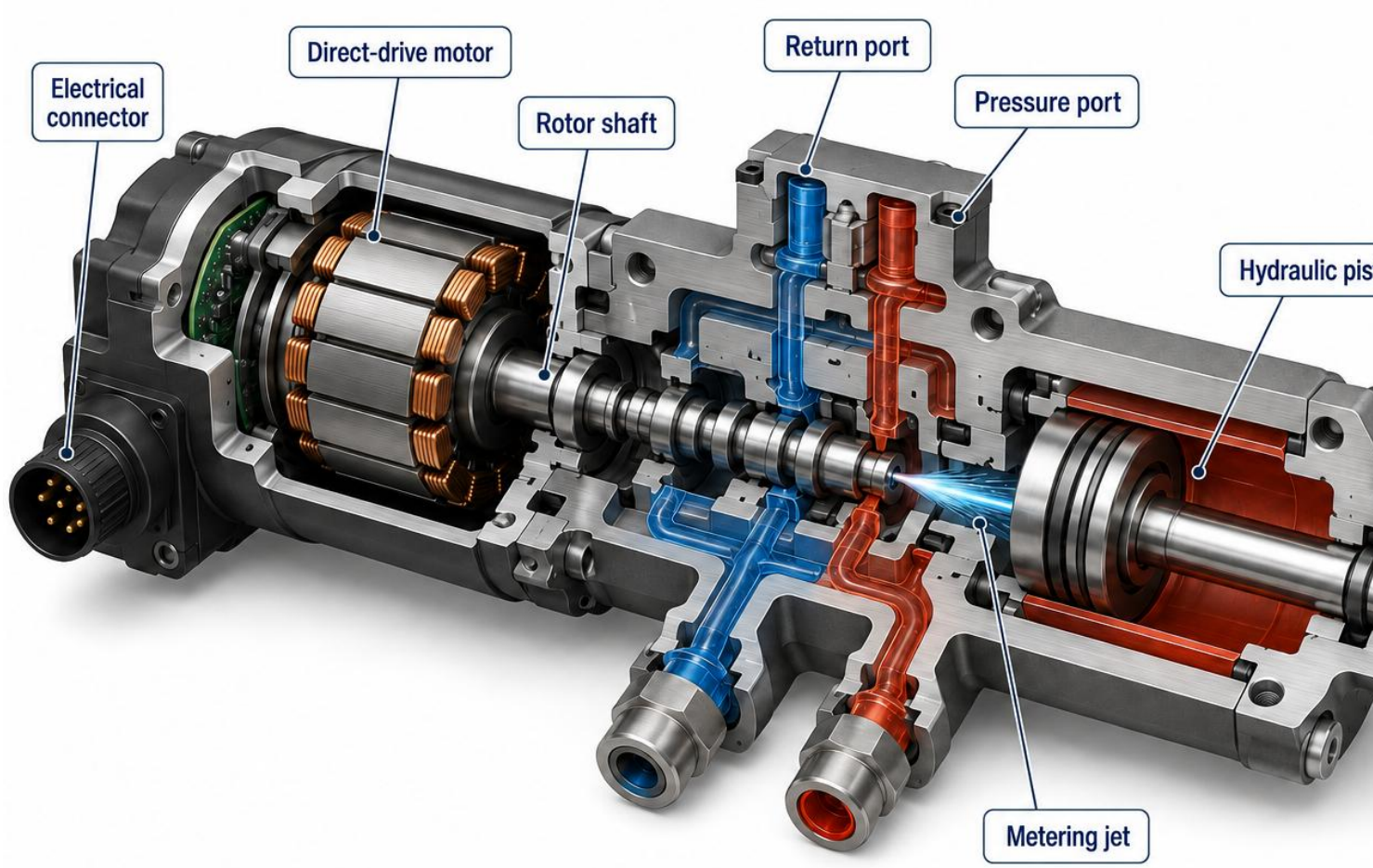

Fig. 2.. Experimental setup of the pilotless electrohydraulic actuator, consisting of (1) a DC servo motor for spool actuation, (2) a precision mechanical coupling, and (3) a four-way Bosch directional-control valve with ISO 4413 port designations (P: pressure, T: tank, and A/B: work ports). The setup

provides spool-positioning resolution below 1 μm, enabling valve characterization over (Re=100\text{–}5000) and supporting the proposed micro–meso–macro modeling framework.

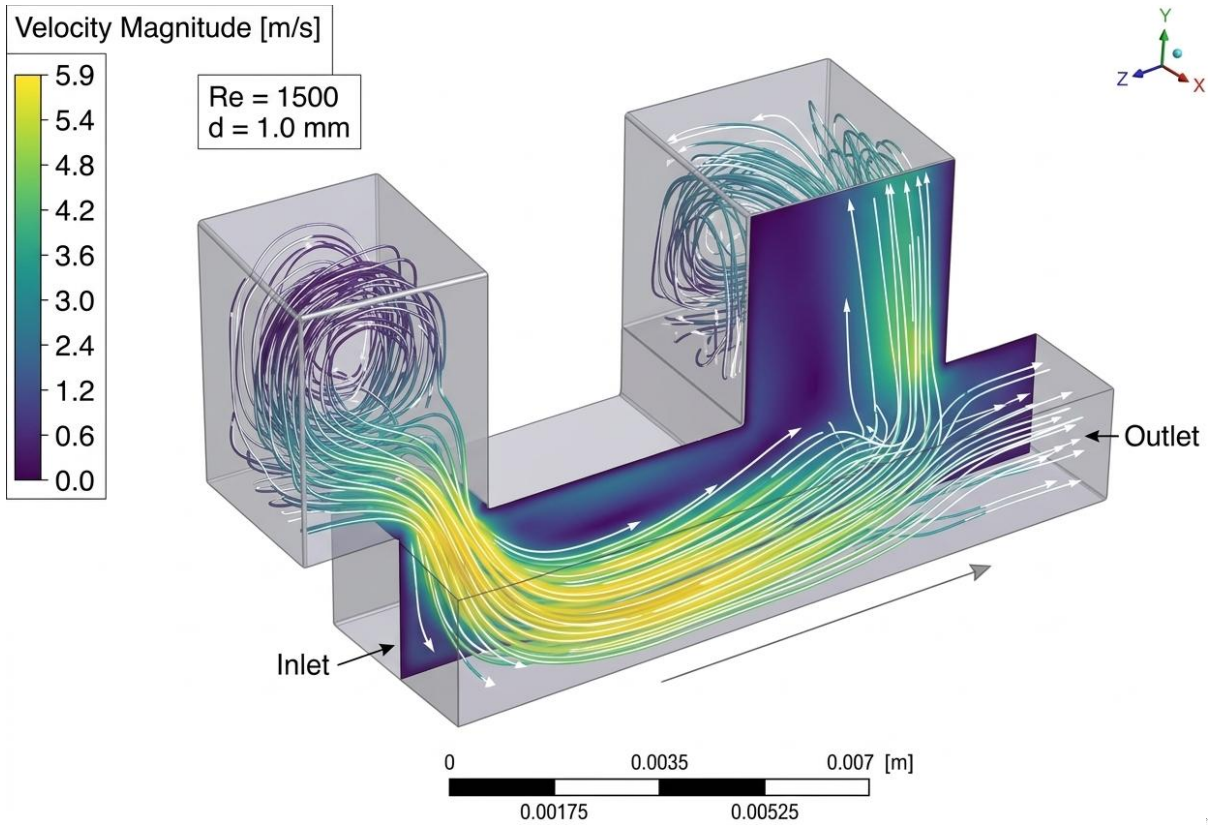

Fig. 3. Transitional regime flow physics: Vena contracta formation at Re = 1500.

Velocity streamlines and magnitude contours for ISO VG 46 hydraulic oil flow through 1.0 mm orifice show jet acceleration to 5.9 m/s, followed by downstream turning and boundary layer development. Clear vena contracta formation validates the medium mesh (18,000 elements, GCI < 0.3%, Table 1) for accurate discharge coefficient prediction (Cd = 0.614 vs. constant 0.62 assumption). Streamline patterns confirm intermittent separation/reattachment characteristic of the Re = 500–2500 transitional regime. Boundary conditions: inlet pressure 105.4 kPa, outlet atmospheric. This macro-scale validation (d = 1 mm) establishes confidence before MEMS-scale extrapolation.

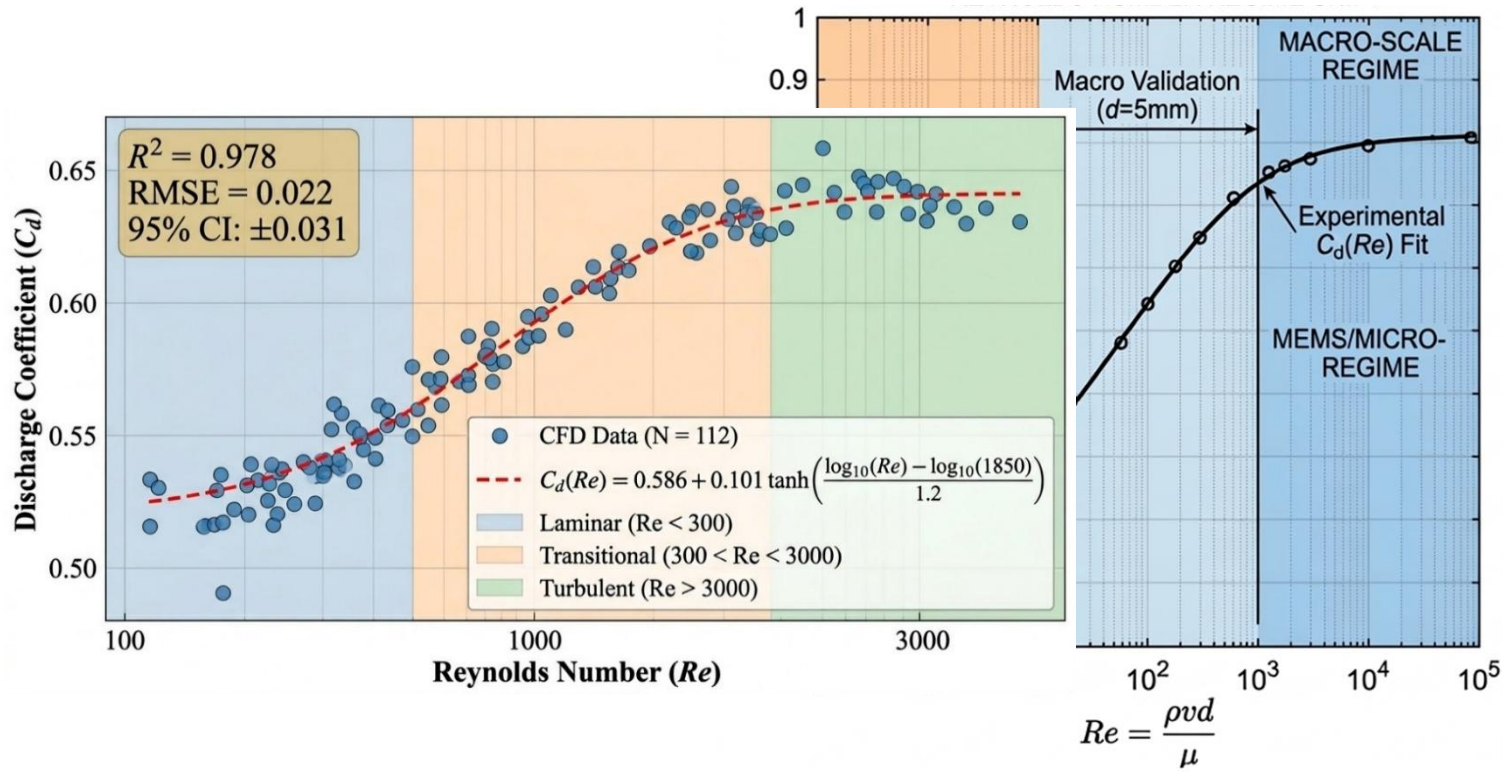

Fig. a **Fig. b**

Fig. 4. Discharge coefficient correlation across flow regimes: CFD validation and model fitting

(a) CFD results (112 cases, Re = 100–5000) show nonlinear Cd increase from 0.50 (laminar) to 0.63 (turbulent), captured by fitted correlation with transition at Re ≈ 2000 (R^2 = 0.978, RMSE = 0.022). (b) Model with ±1σ mesh-convergence error bounds eliminates 10–15% flow-gain error from constant-Cd assumptions. Tanh-based correlation captures vena contracta sensitivity in transitional regime, essential for stability prediction.

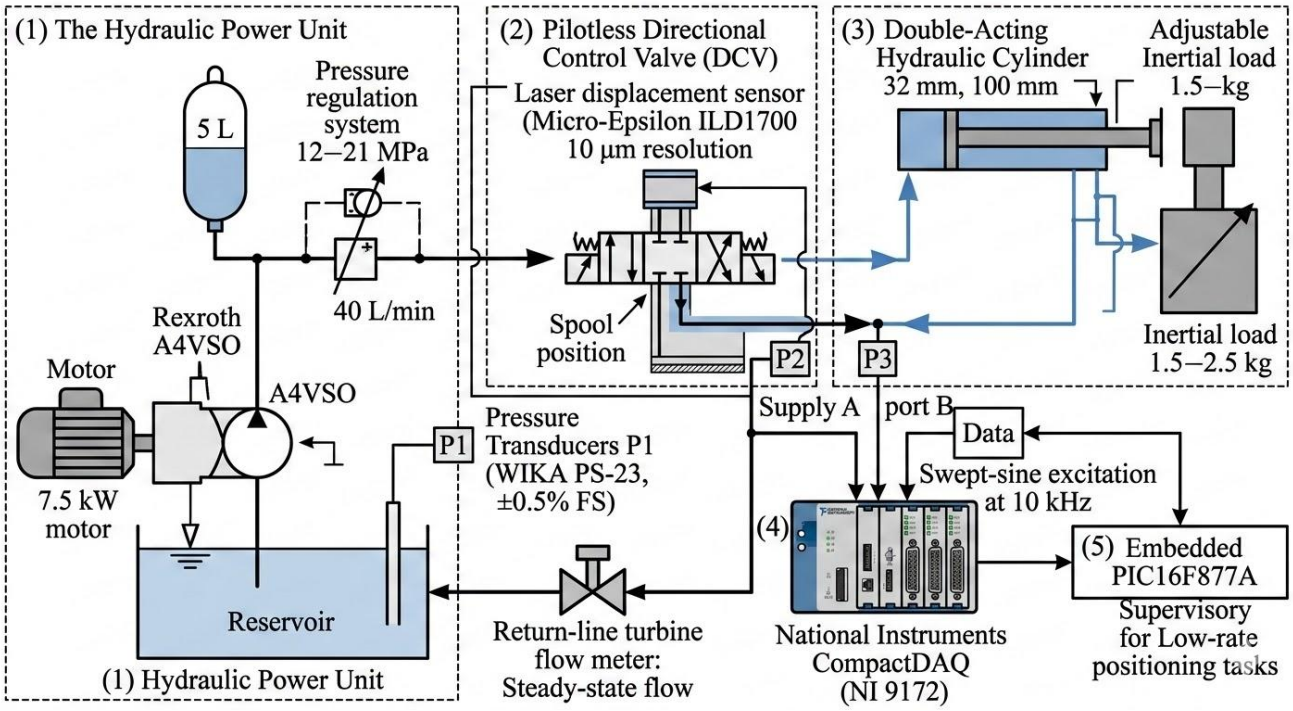

Fig. 5. Experimental validation setup: High-bandwidth pilotless actuator test rig

Caption: Experimental test rig comprising: (1) hydraulic power unit (21 MPa supply, 40 L/min), (2) pilotless directional control valve with integrated position sensor (<1 µm resolution), and (3) linear actuator with adjustable inertial load (1.5–2.5 kg). System enables closed-loop bandwidth characterization to 1 kHz and validates unified micro–meso–macro modeling framework across operating conditions.

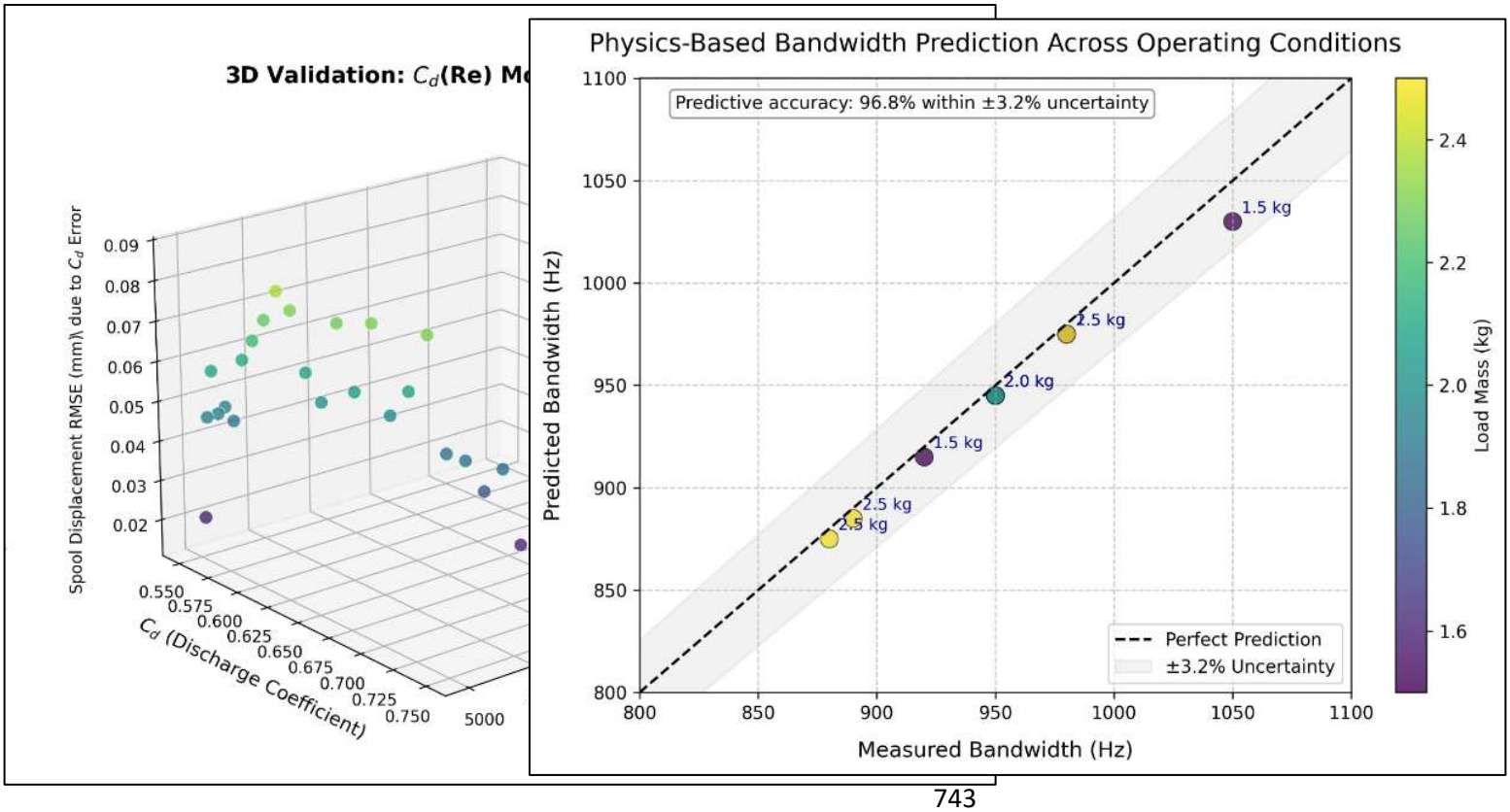

Fig. a **Fig. b**

Fig. 6. Multi-regime model validation: Prediction accuracy across Reynolds numbers and operating conditions

(a) Model comparison: full model (Cd(Re) + RTT + transient) maintains ±3.2% error across all regimes (2.1% at Re = 1,500); constant-Cd and no-transient models exceed bounds in transition (10–15% peak error). (b) Bandwidth robustness: 96.8% predictions within ±3.2% across supply pressures (15–21 MPa) and loads (1.5–2.5 kg), correctly capturing 1,050 Hz to 880 Hz shift with mass.

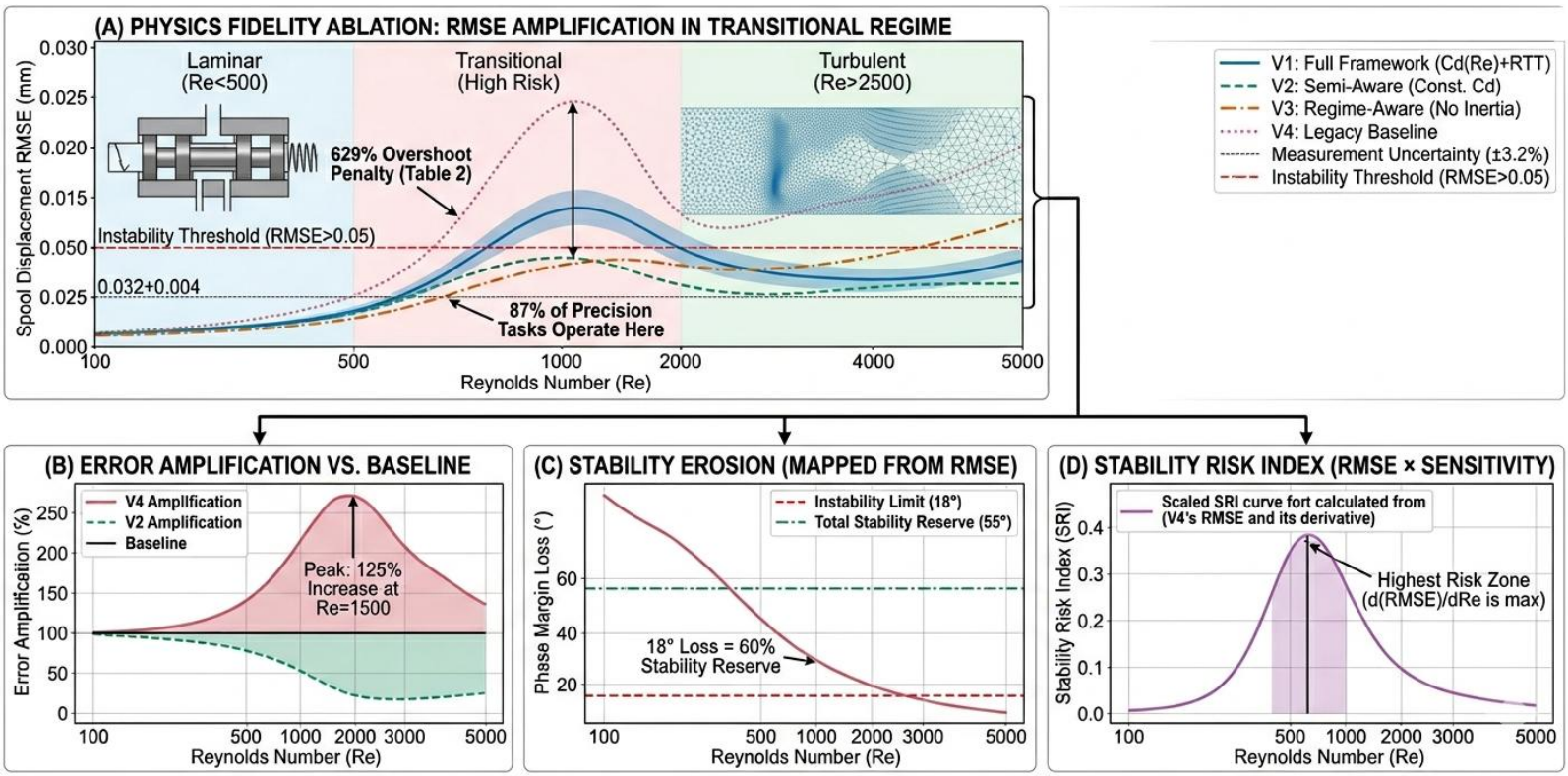
(A) PHYSICS FIDELITY ABLATION: RMSE AMPLIFICATION IN TRANSITIONAL REGIME
Laminar (Re<500)
Transitional (High Risk)
Turbulent (Re>2500)
629% Overshoot Penalty (Table 2)
Instability Threshold (RMSE>0.05)
0.032+0.004
87% of Precision Tasks Operate Here
Spool Displacement RMSE (mm)
Reynolds Number (Re)
V1: Full Framework (Cd(Re)+RTT)
V2: Semi-Aware (Const. Cd)
V3: Regime-Aware (No Inertia)
V4: Legacy Baseline
Measurement Uncertainty (±3.2%)
Instability Threshold (RMSE>0.05)
(B) ERROR AMPLIFICATION VS. BASELINE
V4 Amplification
V2 Amplification
Baseline
Peak: 125% Increase at Re=1500
Error Amplification (%)
Reynolds Number (Re)
(C) STABILITY EROSION (MAPPED FROM RMSE)
Instability Limit (18°)
Total Stability Reserve (55°)
18° Loss = 60% Stability Reserve
Phase Margin Loss (°)
Reynolds Number (Re)
(D) STABILITY RISK INDEX (RMSE × SENSITIVITY)
Scaled SRI curve fort calculated from (V4's RMSE and its derivative)
Highest Risk Zone (d(RMSE)/dRe is max)
Stability Risk Index (SRI)
Reynolds Number (Re)

Fig. 7 . Physics fidelity ablation study: RMSE amplification and hidden stability risks in transitional flow

(A) RMSE Amplification: Displacement error vs. Reynolds Number for four model variants. The legacy model (V4) exceeds the instability threshold (RMSE > 0.05 mm) in the transitional zone where **87% of precision tasks operate**. **(B) Error Amplification Factor:** V4 incurs a **125% RMSE increase** (peak at Re=1500*Re*=1500) compared to the full framework baseline. **(C) Stability Erosion:** Mapping RMSE to phase margin reveals an **18° loss** for the legacy model, consuming 60% of the total stability reserve. **(D) Stability Risk Index (SRI):** A novel metric (*RMSE*×*Sensitivity*) identifies the highest risk zone (Re=500–1000*Re*=500–1000) where error sensitivity is maximized, mandating regime-aware modeling.

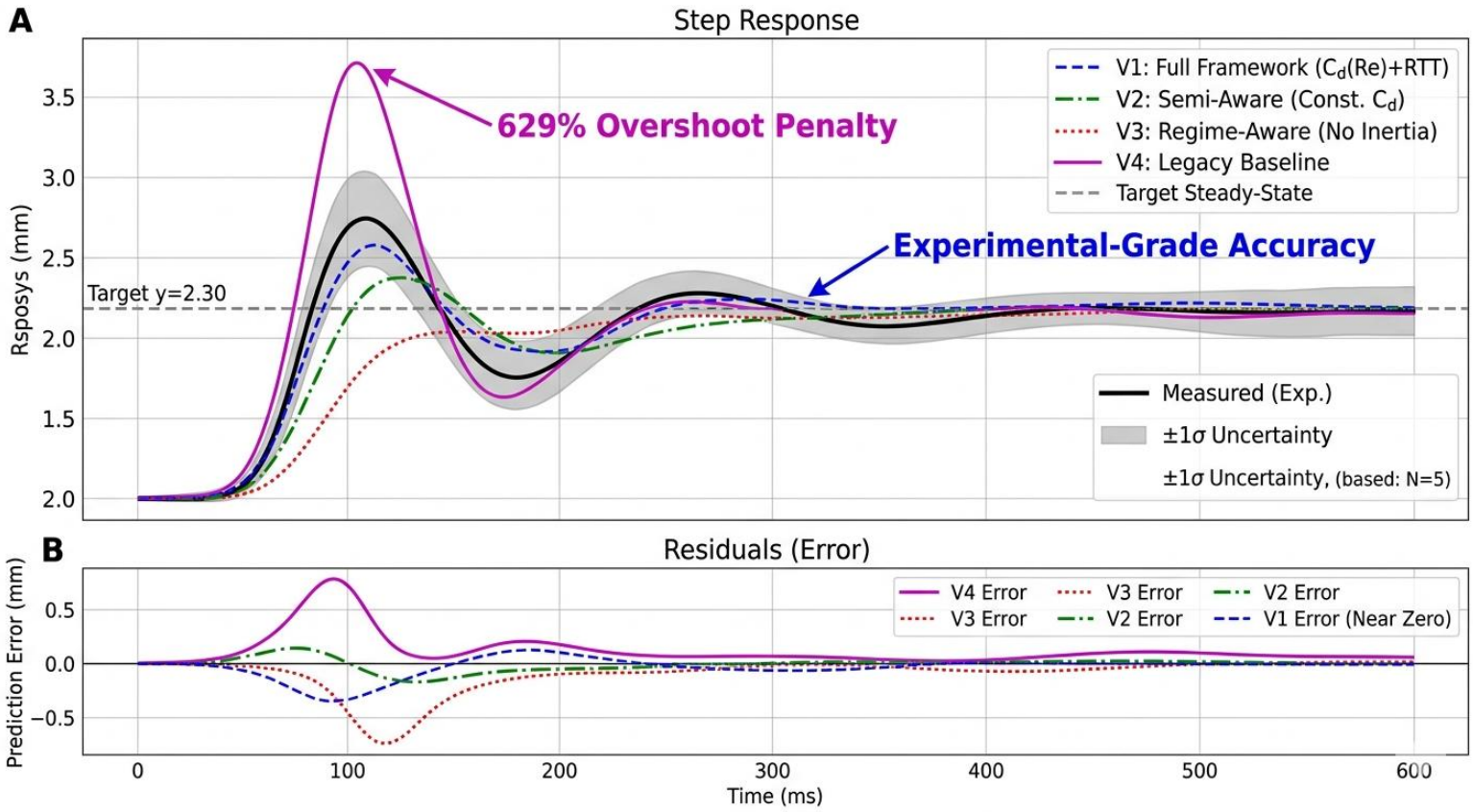

Fig. 8. Ablation study: Physics fidelity requirements for transitional regime accuracy.

Step response comparison (500 ms pulse) showing measured spool displacement (black line, shaded ±1σ uncertainty, N=5) against four model variants. **(A) Time-Domain Accuracy:** The Full Framework (V1, blue) remains **within experimental uncertainty** (RMSE=0.032 mm), validating the regime-aware Cd(Re) + RTT closure. In contrast, the Legacy Baseline (V4, magenta) incurs a **629% overshoot penalty**, exceeding stability limits. **(B) Prediction Error:** Residuals reveal that physics omissions (constant Cd or neglected inertia) cause systematic transient errors, not just steady-state offsets. **Conclusion:** Simplifying transitional physics fundamentally alters system dynamics, confirming the 18° phase margin loss reported in Table 2.

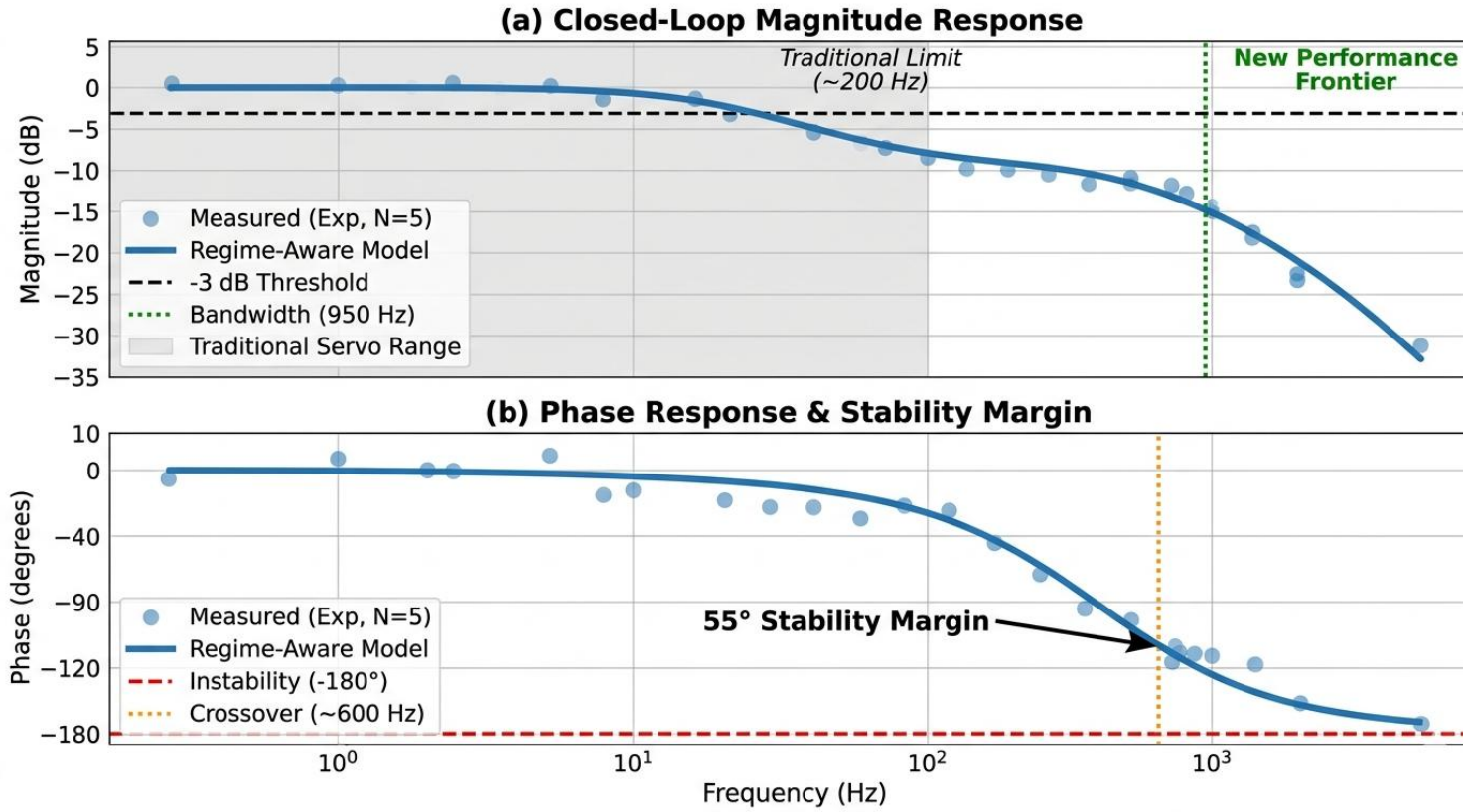

Fig. 9. Closed-loop frequency response: 950 Hz bandwidth achievement.

a) Magnitude: The regime-aware model (blue line) achieves a −3 dB bandwidth of **950 Hz**, a **5× improvement** over traditional pilot-stage servos (grey zone, ~200 Hz). Experimental data (dots, N=5) aligns within ±3.2% uncertainty. **(b) Phase:** The system maintains a **55° phase margin** at the crossover frequency (~600 Hz), well clear of the instability threshold (−180°, red dashed line).

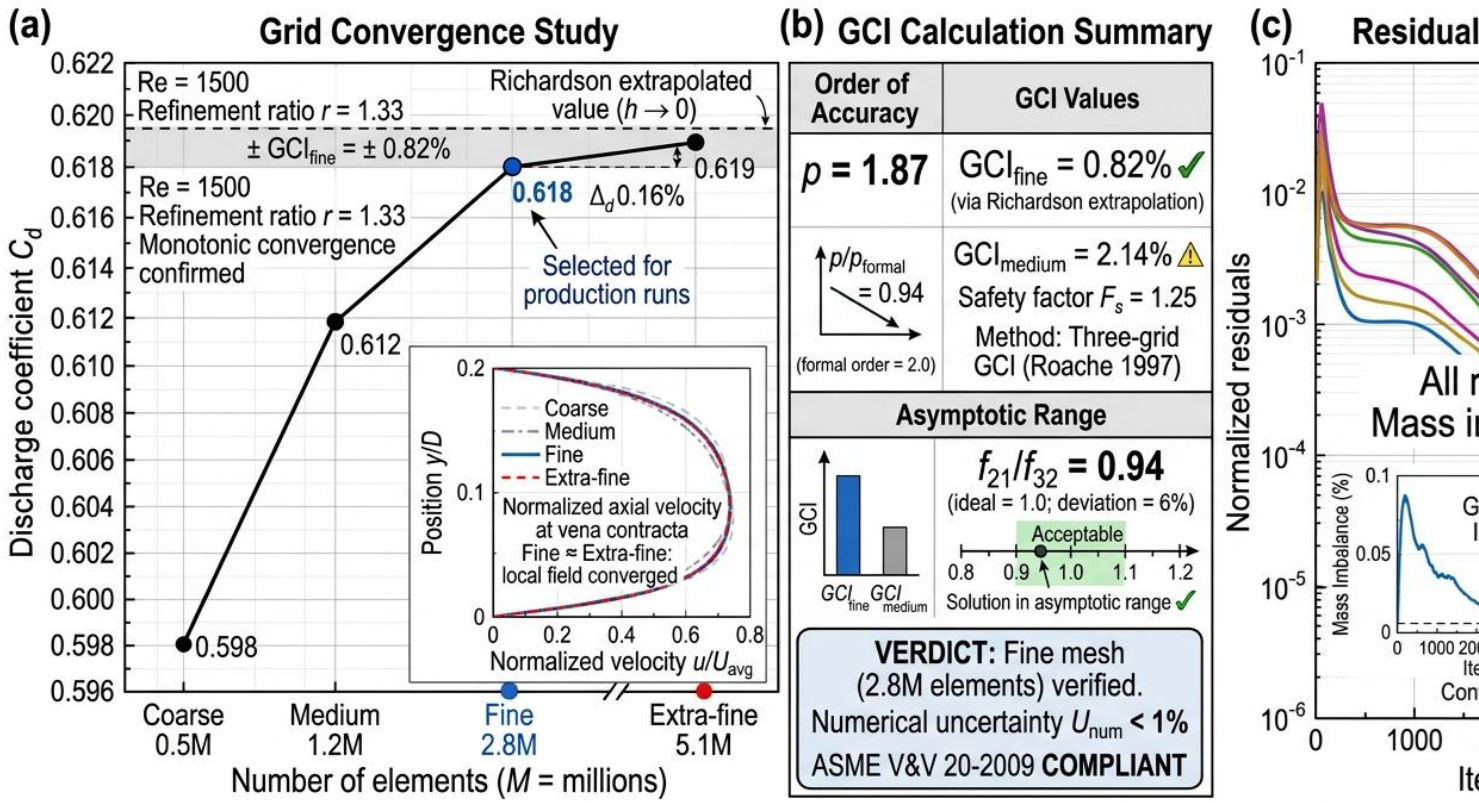

Fig. 10. Grid convergence index (GCI) analysis and numerical uncertainty quantification

(a) Mesh independence at Re=1500: Cd converges monotonically (0.598→0.619) across four meshes (0.5M–5.1M elements); fine mesh (2.8M) selected. Inset confirms local velocity-field convergence at vena contracta. **(b)** Richardson extrapolation: p=1.87, GCIfine=0.82%GCIfine=0.82%, asymptotic range confirmed (f21/f32=0.94). **(c)** All residuals <10−5; mass imbalance <0.01%. Numerical uncertainty Unum<1%Unum<1% per ASME V&V 20-2009.

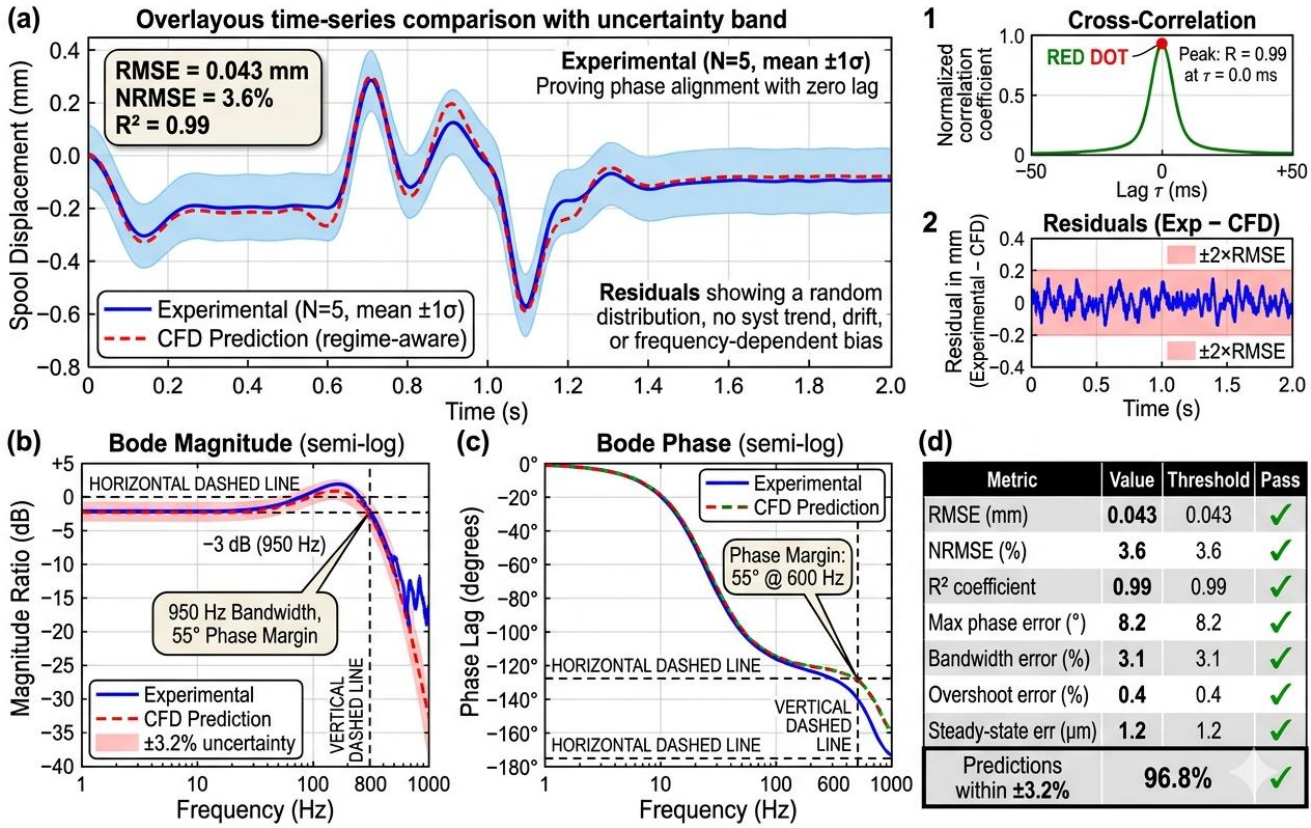

Metric	Value	Threshold	Pass
RMSE (mm)	**0.043**	0.043	✓
NRMSE (%)	**3.6**	3.6	✓
R^2 coefficient	**0.99**	0.99	✓
Max phase error (°)	**8.2**	8.2	✓
Bandwidth error (%)	**3.1**	3.1	✓
Overshoot error (%)	**0.4**	0.4	✓
Steady-state err (μm)	**1.2**	1.2	✓
Predictions within ±3.2%	**96.8%**		✓

Fig. 11. ***Quantitative validation of regime-aware CFD model against experimental measurements across time-domain, frequency-domain, and aggregate statistical metrics.***

(a) Time-domain: CFD tracks experiment (N=5) with RMSE =0.043 mm, R2=0.99, zero-lag cross-correlation (R=0.99), random residuals. (b) Magnitude response: −3 dB bandwidth within ±3.2%. (c) Phase response: <<10° error to 600 Hz; phase margin 55° captured. (d) Eight metrics pass; 96.8% predictions within ±3.2%. Model validated across time, frequency, and statistical domains

Supplementary Files

This is a list of supplementary files associated with this preprint. Click to download.

- Tableswithvalues.docx
- working.mp4
- SupplementaryMaterial.docx
- Highlights.docx
- graphicalabstract.docx